RSC Advances

PAPER

View Article Online
View Journal | View Issue

Cite this: *RSC Adv.*, 2025, **15**, 4120

Engineering the structures of ZnCo-MOFs *via* a ligand effect for enhanced supercapacitor performance†

Kabir Opeyemi Otun, * Ndeye Fatou Diop, Oladepo Fasakin, Rashed Ali Mohamed Adam, Gift Rutavi and Ncholu Manyala *

Tuning the structures, compositions and morphologies of metal–organic frameworks (MOFs) is critical to boosting their supercapacitor performances. In this study, a ligand-engineering strategy was adopted to fabricate ZnCo-bimetallic MOFs with unique properties using three different ligands (2-methylimidazole, terephthalic acid and 2-amino terephthalic acid) under the same synthesis protocol. The variation in the electron-donating ability of the three ligands gave rise to changes in their structural, morphological and electrochemical properties. Compared to other MOFs, the imidazole-based ZnCo-MOF (ZnCo-MOF-HMIM) with a dodecahedron morphology, good specific surface area and moderate pore characteristics provided considerable electron transport paths for ion migration on the electrode surface site, which guarantees a greater charge storage. Specifically, ZnCo-MOF-HMIM delivered the best specific capacity of 176.8 m h A g^{-1} at 1 A g^{-1} specific current and retains about 87.5% of its capacity at 10 A g^{-1} after 5000 cycles. Furthermore, the asymmetric device achieved a specific energy of 28.2 W h kg^{-1} at a specific power of 1025.4 W kg^{-1} and demonstrates remarkable coulombic efficiency and capacity retention of 98.4% and 80.0% at 10 A g^{-1} over 10 000 cycles respectively. The presence of an N donor atom in the imidazole ligand which imparts high hydrophobicity, and the synergistic effects of Zn and Co ions could predispose ZnCo-MOF-HMIM to have more active sites and greater stability for enhanced performance. This work provides insight into the key role of ligands in the formation mechanism of bimetallic MOFs for enhanced electrochemical energy storage.

Received 18th November 2024
Accepted 31st January 2025

DOI: 10.1039/d4ra08192g

rsc.li/rsc-advances

1. Introduction

Exploiting environmentally friendly and sustainable energy storage technologies is challenging given the surge in the demand for renewable energy resources and the continuous exhaustion of fossil fuels.[1] Supercapacitors play a significant role in the realms of renewable energy and environmental sustainability.[2] In the renewable energy context, supercapacitors serve as key components of energy storage systems.[3] Their tendency to store and release energy rapidly makes them suitable to disentangle intermittent renewable energy sources to deliver a consistent and reliable energy supply.[4] In addition, supercapacitors have fast charge–discharge capability, high specific power, long cycle life, and reduced ecological footprint which make them environmentally benign.[5] Supercapacitors (SCs) can either be electrical double-layer capacitors or pseudocapacitors depending on the mechanism of storage, with the latter having a higher specific capacitance.[6] Pseudocapacitors have drawn considerable interest for supercapacitor applications because of their high electron transport efficiency and quick mass transfer. They also provide high charge storage in a short amount of time because of fast redox processes.[7] Presently, carbon-based materials are the leading materials employed as electrodes in supercapacitors.[8–10] However, a major barrier to their widespread usage is their low theoretical specific capacitance.[11] As such, the development and fabrication of supercapacitor electrodes with high capacity, exceptional rate potential and extended cycle stability is necessary.[12]

Metal–organic frameworks (MOFs), which came to the limelight about three decades ago, have advanced supercapacitor performance owing to their fascinating features including abundant coordination sites, high surface areas, adjustable pore characteristics and ease of tunability.[13] The coordination of organic ligands with metal ion nodes/clusters produces MOFs, which are porous hybrid networks whose textural and structural features may be tuned for SCs by varying the metal and linker combinations.[14] Combining the advantages of the inorganic metal nodes with redox activity and organic building units, MOFs can occupy a place in the search of novel electrodes for supercapacitors. However, due to their limited stability and low electrical conductivity, pristine MOFs

Department of Physics, Institute of Applied Materials, University of Pretoria, 0001, Pretoria, South Africa. E-mail: otunkabir2705@gmail.com; ncholu.manyala@up.ac.za

† Electronic supplementary information (ESI) available. See DOI: https://doi.org/10.1039/d4ra08192g

have limited applications in supercapacit.[15] One of the facile and promising approaches to get rid of this limitation is to add a second or a third component to the pristine MOFs to make MOF composites which can improve the stability and conductivity *via* a synergistic effect between the metal components.[16] For example, Wang *et al.*[17] designed ultrathin NiCo-MOF nanosheets in an ultrasonic synthesis for a supercapacitor electrode, and delivered a high specific capacitance of 1202 F g^{-1} at 1 A g^{-1}, surpassing the specific capacitance of pristine Ni-MOFs. This performance was credited to the distinct design of the bimetallic MOF and the combined action of two metal components, which offer considerable electroactive sites and shorter pathways for the passage of electrons and electrolyte.[17] Yu *et al.* also explored the design of an iron-doped Co-MOF for supercapacitors. The bimetallic MOF, which benefits from the presence of two metals, has the maximum specific capacitance with remarkable stability, measuring 319.5 F g^{-1} at 1 A g^{-1}, 1.4 and four times that of pristine Co-MOF (210.5 F g^{-1}) and Fe-MOF (78.8 F g^{-1}), respectively.[18]

Furthermore, recent studies have shown that the choice of organic ligands is essential for adjusting the morphology, porosity, and structural design of MOFs, especially for MOFs with identical metal nodes.[19] For instance, He *et al.*[20] prepared four La-based MOFs using different linkers and found that the organic linkers significantly influenced the morphology, pore characteristics, and the phosphate adsorption properties of the MOF materials. Murugan *et al.*[21] reported ligand mediated self-assembly of cobalt nanoclusters *via* a simplistic one-step synthesis method to design a hybrid device. They found out that different ligands displayed different supercapacitor performance depending on the flexibility and electron-donating capability of the ligands. The rigid-dense multifunctional ligand, glutathione, delivered remarkable specific capacitance of 540 F g^{-1} at 1 A g^{-1}.[21] Despite the remarkable progress in the effects of linkers on MOF performance, it is crucial to note that the ligand effects on MOFs have been largely restricted to single metal MOFs, which have been implicated to have limited performance in supercapacitors. This limitation leaves ample room for further research, especially the magnitude of interactions among the ligands of interest with dual transition metal ions to produce various reactions and structures needs to be studied.

Inspired by the above considerations, we selected three different organic linkers to tune the structures and morphologies of ZnCo-bimetallic MOFs for supercapacitors. The linkers (whose structural details are given in Table S1†) include HMIM = 2-methylimidazole (with N-donor atom embedded in the imidazole ring attached to a hydrophobic $-CH_3$ group), BDC = 1,4-benzenedicarboxylic acid (with O-donor atom), and ABDC = 2-amino-benzenedicarboxylic acid (with free O and N- donor atoms). The ZnCo-MOF-HMIM, ZnCo-MOF-BDC and ZnCo-MOF-ABDC MOFs were synthesized by adding the nitrate salts of Zn^{2+} and Co^{2+} to the corresponding organic linkers under solvothermal conditions, and evaluating their charge storage performance. The addition of Zn into the Co-based MOF improves the concentration of unpaired electrons and augments the redox activity of Co^{2+}, which serve as electrochemical active species. When compared to other MOFs, the Zn^{2+} and Co^{2+} ions in ZnCo-MOF-HMIM penetrate the MOF to synergize the bimetallic active sites through the unique coordination of the N donor atoms from the imidazole ligand which combines high hydrophobicity. As such, ZnCo-MOF-HMIM delivered the best specific capacity of 176.8 m h A g^{-1} at a specific current of 1 A g^{-1} and retains about 87.5% of its capacity at 10 A g^{-1} after 5000 cycles. The asymmetric device assembled using ZnCo-MOF-HMIM and activated carbon at a cell potential of 1.60 V demonstrated a specific energy of 28.2 W h kg^{-1} at a specific power of 1025.4 W kg^{-1}, and retains 80.0% of its initial capacity over at 10 A g^{-1} over 10 000 cycles. This work gives insight into engineering the structures of bimetallic MOFs *via* ligand effects for enhanced electrochemical energy storage performance.

2. Experimental

2.1 Materials

Zinc nitrate hexahydrate [$Zn(NO_3)\cdot 6H_2O$], cobalt nitrate hexahydrate [$Co(NO_3)_2\cdot 6H_2O$], terephthalic acid (H_2BDC), 2-aminoterephthalic acid (NH_2–H_2BDC) and 2-methyl imidazole (2-HMIM) were supplied by Merck and used without additional purification. Others such as KOH, *N*,*N*-dimethylformamide (DMF), ethanol, and *N*-methylpyrrolidone were procured from Fischer Chemical Ltd.

2.2 Preparation of ZnCo-MOFs with three different ligands

The ZnCo-MOFs were synthesized by co-precipitating $Co(NO_3)_2\cdot 6H_2O$ and $Zn(NO_3)\cdot 6H_2O$ using an appropriate organic linker in a hydrothermal synthesis at 120 °C in methanol and DMF solvent system (3 : 1 v/v). Typically, 1.2 mmol of $Zn(NO_3)\cdot 6H_2O$ and $Co(NO_3)_2\cdot 6H_2O$ were dissolved in DMF to make solution A. Then, terephthalic acid was dissolved in a mixture of ethanol and DMF to make solution B. Following a 15 minutes ultrasonic agitation to ensure total dissolution, solution A was added to solution B. After that, the mixture was heated to 120 °C for 12 hours in a 50 mL stainless-steel autoclave lined with Teflon. Bimetallic ZnCo-MOF-BDC was obtained by centrifuging the precipitate, washing repeatedly with DMF and ethanol, and then drying it for an entire night at 70 °C in a vacuum oven following crystallization and cooling. To investigate the effects of ligand, similar reaction conditions were maintained except for the use of 2-aminoterephthalic acid and 2-methylimidazole in the place of terephthalic acid to produce ZnCo-MOF-ABDC and ZnCo-MOF-HMIM, respectively.

2.3 Characterization

The phase crystallinity was assessed using an X-ray diffractometer (XRD, Philips PW-1710). The materials' surface morphologies and elemental compositions were examined using a scanning electron microscope (SEM) coupled to an energy dispersive spectrometer (EDS), and the structural morphology was captured using a transmission electron microscope (TEM, JSM-2100F). The specific surface area and related pore size distribution of the samples were investigated

using nitrogen adsorption–desorption isotherms (Micromeritics ASAP 2460, USA) that incorporate the Brunauer–Emmett–Teller (BET) approach and the Barrett–Joyner–Halenda (BJH) model. The examination of Raman spectroscopy was performed using the WITec alpha-300 RAS^{+} Confocal micro-Raman microscope. The thermogravimetric analysis. Nicolet 750 FTIR spectrometer (Bruker) was used to measure the Fourier transform infrared (FTIR) spectra of the materials in the absorption mode. An SMP/PF7548/MET/600 W instrument was used to perform thermal gravimetric analysis (TGA) in a nitrogen environment at temperatures between 50 and 800 °C ramped at 10 °C min^{-1}.

2.4 Electrode preparation

The electrode materials involving the ligand-modified ZnCo-MOFs were synthesized by mixing the active material (ZnCo-MOF) with acetylene black as a conductive material, and PVDF as a binder in a mortar at a mass ratio of 8 : 1 : 1, respectively. The mixture was homogeneously ground with the addition of a suitable amount of NMP to obtain a slurry. The slurry was then applied on a pre-cleaned Ni-foam current collector covering the surface of 1 cm × 1 cm and oven dried at 60 °C for 12 h. The mass loadings of ZnCo-MOF-HMIM, ZnCo-MOF-BDC and ZnCo-MOF-ABDC are 3.0, 2.5 and 3.2 mg respectively.

2.5 Electrochemical characterization

Electrochemical evaluations were all carried out at ambient temperature using the bimetallic ZnCo-MOF electrodes, a Ag/AgCl electrode, and a glassy carbon as working, reference, and counter electrodes, respectively. The electrochemical characterization, such as cyclic voltammetry (CV), galvanostatic charge–discharge (GCD) as well as electrochemical impedance spectroscopy (EIS) measurements were measured on a Bio-logic VMP-300 electrochemical workstation in a conventional three- and two-electrode system configurations using 6 M KOH electrolyte solution. For three-electrode, the CV tests of the three ZnCo-bimetallic MOFs (ZnCo-MOF-HMIM, ZnCo-MOF-BDC and ZnCo-MOF-ABDC) were taken within the potential window range of 0.0 and 0.5 V at different scan rates ranging from 5 to 100 mV s^{-1}. The GCD curves were taken in the voltage range of 0.0 to 0.4 V, while the EIS was obtained in the frequency range of 100 kHz to 0.01 Hz at an open circuit potential.

The specific capacity, Q_S at different specific currents was calculated from the GCD curves using eqn (1):[22]

$$Q_S(\text{mA h g}^{-1}) = \frac{I \times \Delta t}{3.6m} \quad (1)$$

Moreover, the specific energy (W h kg^{-1}) and specific power (W kg^{-1}) of the assembled device are computed using eqn (2) and (3) respectively.[23]

$$E_S = \frac{I}{3.6(m_+ + m_-)} \int V(t)\mathrm{d}t \quad (2)$$

$$P = \frac{3600E_S}{\Delta t} \quad (3)$$

In the eqn (2), $\int V(t)\mathrm{d}t$ is the GCD test curve area with respect to the discharge time, while m_+ and m_- are the mass loadings of the positive and negative electrode, while Δt in eqn (3) is the discharge time.

3. Results and discussion

The electrode materials involving the three ligands under test were synthesized by a single-step solvothermal approach as demonstrated in Scheme 1. The different ligands (HMIM, BDC

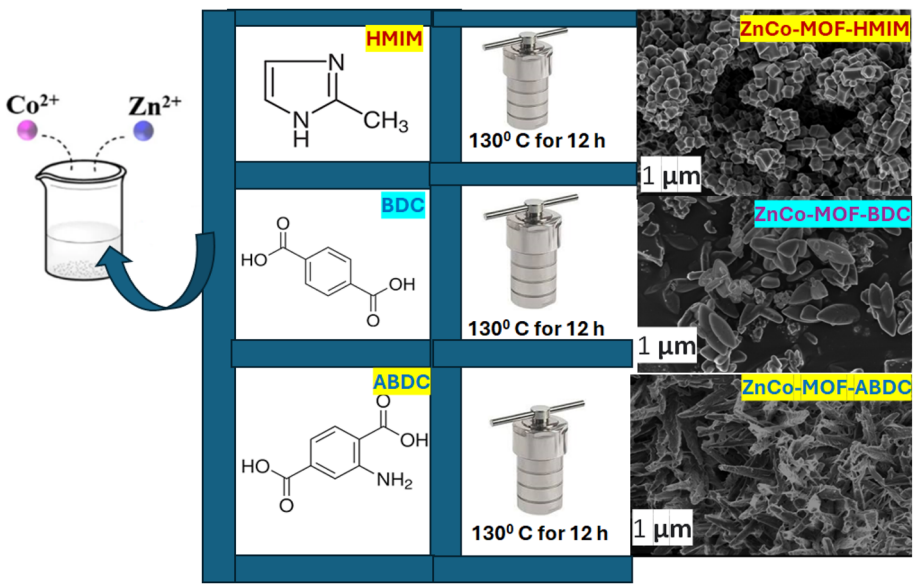

Scheme 1 The scheme illustrating the preparation process of bimetallic ZnCo-MOF-HMIM, ZnCo-MOF-BDC and ZnCo-MOF-ABDC using ligand effect.

and ABDC) were coordinated in different manners to Zn^{2+} and Co^{2+}, which possess identical chemical valence states, ultimately leading to interconnected bimetallic ZnCo-MOFs with different structural architecture and morphology.

The structural phase of the of the ZnCo-MOFs modified by linker effect was assessed by the XRD and the result is displayed in Fig. 1a. The spectra showed that the incorporation of various organic ligands altered the structures of the resulting MOFs with each of the MOFs exhibiting high crystallinity without amorphous peaks. The peaks were matched with the corresponding linkers and there was a minor peak shift of the linkers upon incorporation of the Zn^{2+} and Co^{2+} ions. The sharp peaks at $2\theta = 10.8$ and 14.3° for all the three ZnCo-MOFs are linked to the (011) and (112) crystal planes for Zn-MOF and Co-MOF, respectively.[24] Additionally, the peaks were observed for ZnCo MOF_HMIM at 13.01, 15.13, and 23.92°, equivalent to the (101), (200), and (020) crystal planes of Zn-MOF (JCPDS: 23-1390).[25] The 2-methylimidazole (HMIM) ligand is the source of the peaks for ZnCoMOF-HMIM at 17.72, 25.92 and 36.08° (JCPDS: 23-1030).[26] Furthermore, the presence of benzene-carboxylic acid and amino benzene carboxylic acid coordination is confirmed by the peaks for ZnCoMOF-BDC and ZnCoMOF-ABDC respectively at 17.31, 25.25 and 27.62° and 14.51, 26.72 and 39.4°.[27] The XRD patterns confirmed the successful preparation of the ZnCo-MOFs with the three different organic ligands, and the obvious differences in their structures may impact their morphologies and their overall supercapacitor performance.

Raman spectroscopy was used to investigate the structure-related alterations resulting from linker–metal interactions with various ligands in ZnCo-MOFs. Two primary band group sections are visible in the Raman spectra of ZnCo-MOF-HMIM, ZnCo-MOF-BDC, and ZnCo-MOF-ABDC shown in Fig. 1b. These are 800–880 cm^{-1} and 1200–1620 cm^{-1} bands. The bands at 1416, 1455, 1563, and 1612 cm^{-1} are visible in the 1200–1620 cm^{-1} range. These positions can be ascribed to the symmetric $\nu(COO^{-})$, and benzene rings, respectively.[28] The carboxylate group of the organic linkers from ZnCo-MOF-BDC and ZnCo-MOF-ABDC can be stretched in two different ways: symmetrically at 1416 and 1455 cm^{-1} and asymmetrically at 1563 and 1612 cm^{-1}. Lower wavenumber bands, around 680 cm^{-1}, could be the result of vibrations caused by bending and deformation of the benzene and imidazolate rings, respectively. The extra bands located at 416, 456 and 475 cm^{-1} might result from metal–O and metal–N ligand bond vibrations. Comparison of the Raman spectra of the three MOFs showed that the three bimetallic MOFs resulted from different interactions of the metals with the ligands.

As a complementary technique to Raman, FTIR was employed to assess the bonding and structural compositions of the ligand-mediated bimetallic ZnCo-MOF. As shown in Fig. 2a, The FTIR spectra of ZnCo-MOF-HMIM peak at 3508 cm^{-1} indicating the N–H stretch vibration from the imidazolate ligand. Furthermore, it was determined that the stretching of the –COO– groups in the terephthalate anions were attributed to the distinctive peaks at 1585, 1548 and 1362 cm^{-1}. The amine

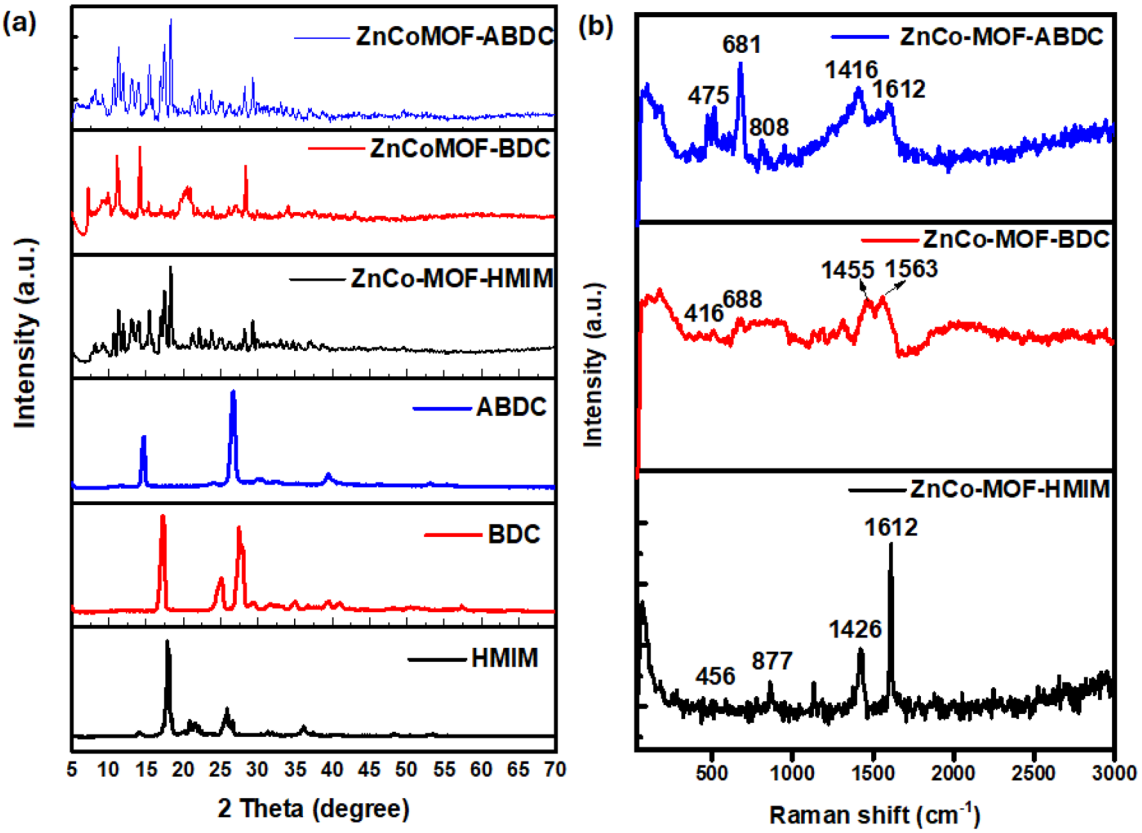

Fig. 1 (a) X-ray diffraction patterns and (b) Raman spectra of ZnCoMOF-HMIM, ZnCoMOF-BDC, and ZnCoMOF-HMIM.

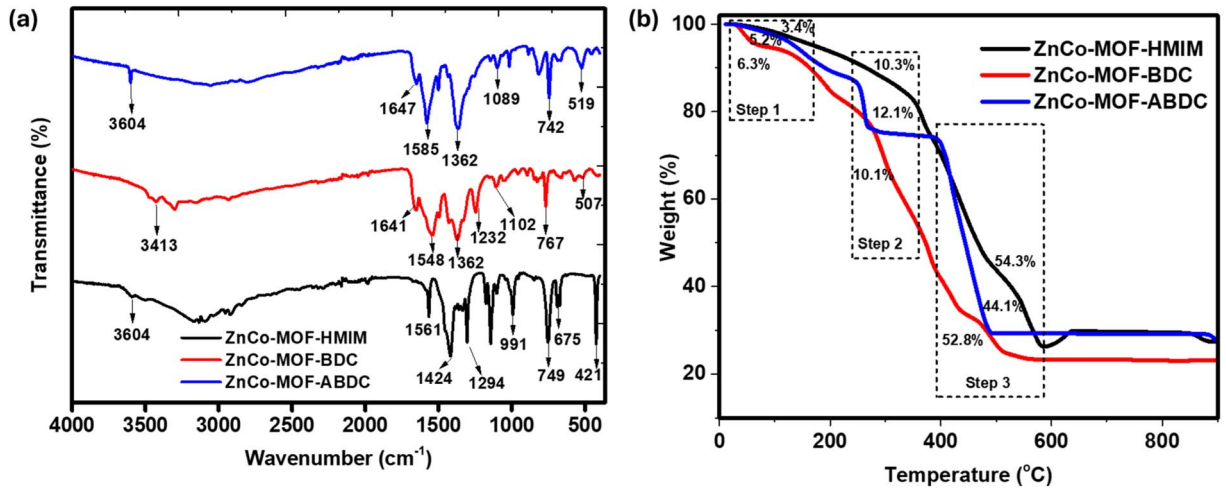

Fig. 2 (a) FTIR spectra and (b) TGA profile of ZnCoMOF-HMIM, ZnCoMOF-BDC, and ZnCoMOF-HMIM.

functional groups of ZnCo-MOF-ABDC showed a sharp peak at 3413 cm^{-1} which is linked to the asymmetrical stretching vibrational mode. The bands positioned at 1561 and 1294 cm^{-1} belong to the N–H bending and C–N bond present in the imidazole ring of ZnCo-MOF-HMIM, respectively. Moreover, the vibrational peaks appearing around 421, 507, 519, 675 and 767 cm^{-1} are associated with the M–O or M–N (M = Zn and Co), carboxylate O=C=O group, and C=C stretching, respectively.[29] The successful structural changes in ZnCo-MOF *via* ligand effect is demonstrated by these FT-IR spectroscopic measurements.

For any material to have a practical and scalable application, it must have high thermal stability. TGA is a technique used to study thermal steadiness and sample composition.[30] The study examined the thermograms of ZnCo-MOF-HMIM, ZnCo-MOF-BDC and ZnCo-MOF-ABDC. A three-stage mass loss profile can be seen in the TGA curves for all the samples shown in Fig. 2b; mass loss from the evaporation of volatile components such as water and trapped guest molecules, framework breakdown, and material decomposition. The ZnCo MOF-HMIM exhibits a higher rate of volatile component evaporation than the other MOFs, with a rate of about 10.8%. This indicates the existence of substantially volatile constituents that are either physisorbed or chemisorbed to the materials of interest. Moreover, the ligand framework begins to decompose and combust at 410 and 590 °C, respectively, for ZnCo MOF-HMIM, which is superior to the other MOF structures in terms of breakdown and combustion temperature. For ZnMOF-BDC, the first region, between 90 and 180 °C, showed 15.4% moisture loss trapped into the pores of MOFs during synthesis. The second area, between 180 °C and 300 °C, experienced a 13% mass loss due to Zn^{2+} and Co^{2+} oxidation. The third region, starting at 300 °C, saw the MOF decompose and combust the organic linker (BDC), and the loss was complete at 455 °C. The decomposition and combustion of ZnMOF-ABDC MOF occur at 450 and 550 °C respectively.

This result aligns with some of the findings in the literature.[31,32] The high stability observed for the ZnCo-HMIM emanates from the strong bond between the 2-methylimidazolate linker and zinc and cobalt ions coupled with the hydrophobic $-CH_3$ group.

Fig. 3a–c shows the SEM images of the bimetallic ZnCo MOFs prepared by using various organic ligands. The SEM micrographs in Fig. 3 show that their morphology and sizes are entirely different. ZnCo-MOF-HMIM exhibited a dodecahedron morphology (Fig. 3a), ZnCo-MOF-BDC is cross-like (Fig. 3b), while that of ZnCo-MOF-ABDC is closely packed elliptical rods (Fig. 3c). The high-magnification SEM images, which display a comparable and homogeneous development of the MOFs are exhibited in Fig. 3d–f. The changes observed in their morphology emanated from their structural differences as confirmed by the XRD, FTIR and Raman spectra. For ZnCo-MOF-HMIM, the dodecahedron's particle size of 356 nm is obtained, which is in the size range of dodecahedron-shaped Co-MOF prepared by Wang and Guo.[33] The EDS mapping also shows that the elements C, O, N, Co and Zn are even distributed in the sample as depicted in Fig. 3g–k.

The corresponding particle size distribution curve is shown in Fig. S1.† This helps to improve charge-storage performance by creating open areas for adsorbing the charges and quick ion movement. The elemental mapping pictures of ZnCo-MOF obtained using energy-dispersive spectroscopy (EDS) (Fig. 4a–c) demonstrate the consistent spreading of C, O, N, Zn, and Co elements in the sample. It is worth noting that ZnCo-MOF-HMIM and ZnCo-MOF-ABDC contain an N element, which fits to the 2-methylimidazole and amine group respectively. However, with ZnCo-MOF-BDC, the N atom on the surface totally vanishes due to the nature of the terephthalic acid ligand that makes up its structure. This suggests that the Co and Zn ions effectively coordinated to the linkers differently to produce corresponding bimetallic MOFs.

Transmission electron microscopy helps to further examine the morphology of the ZnCo-based MOFs in more detail (Fig. 5a–f). The ZnCo-MOF-HMIM features an octahedron structure with smooth surface, as seen in Fig. 5a. ZnCo-MOF-BDC elliptical cross-like morphology was seen in Fig. 5b,

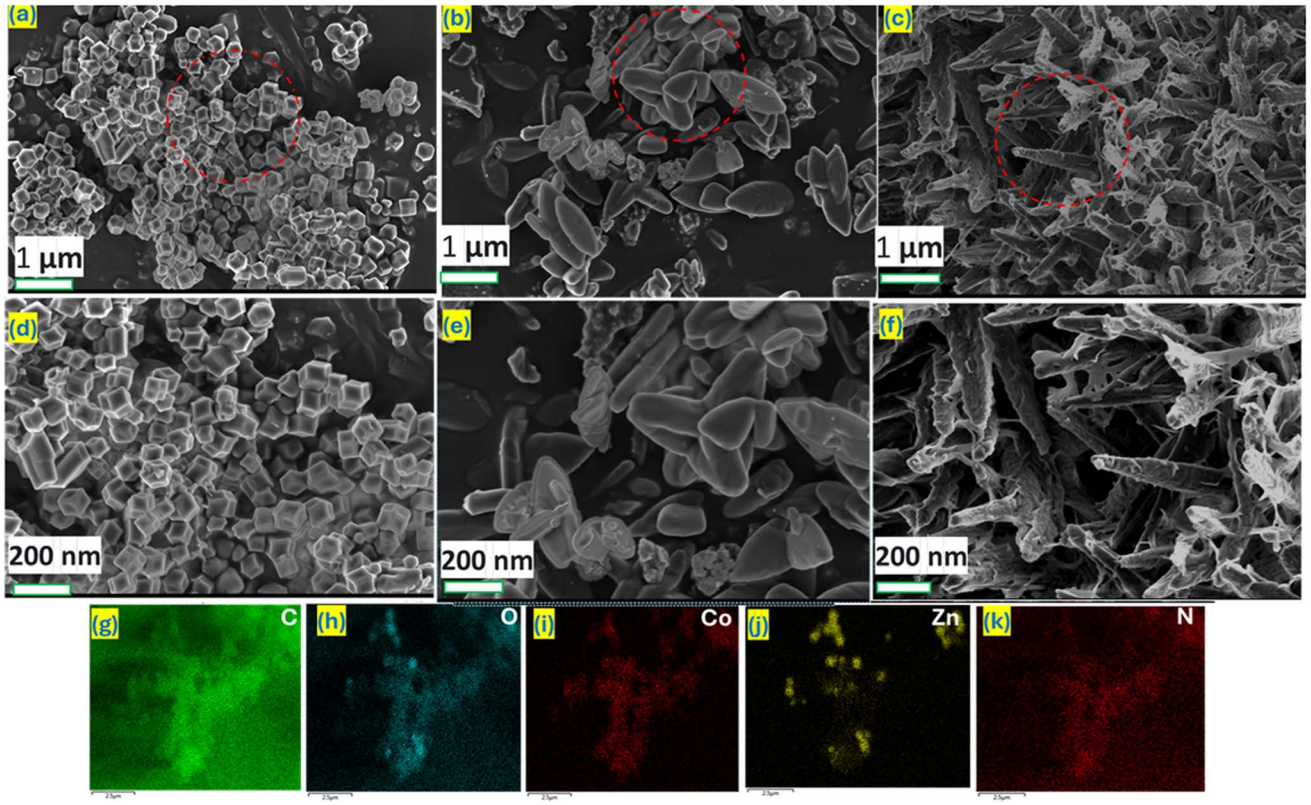

Fig. 3 (a–f) SEM micrographs at various magnifications of (a and d) ZnCo-MOF-HMIM (b and e) ZnCo-MOF-BDC and (c and f) ZnCo-MOF-ABDC, (g–k) EDS mapping of ligand mediated ZnCo-MOF-HMIM.

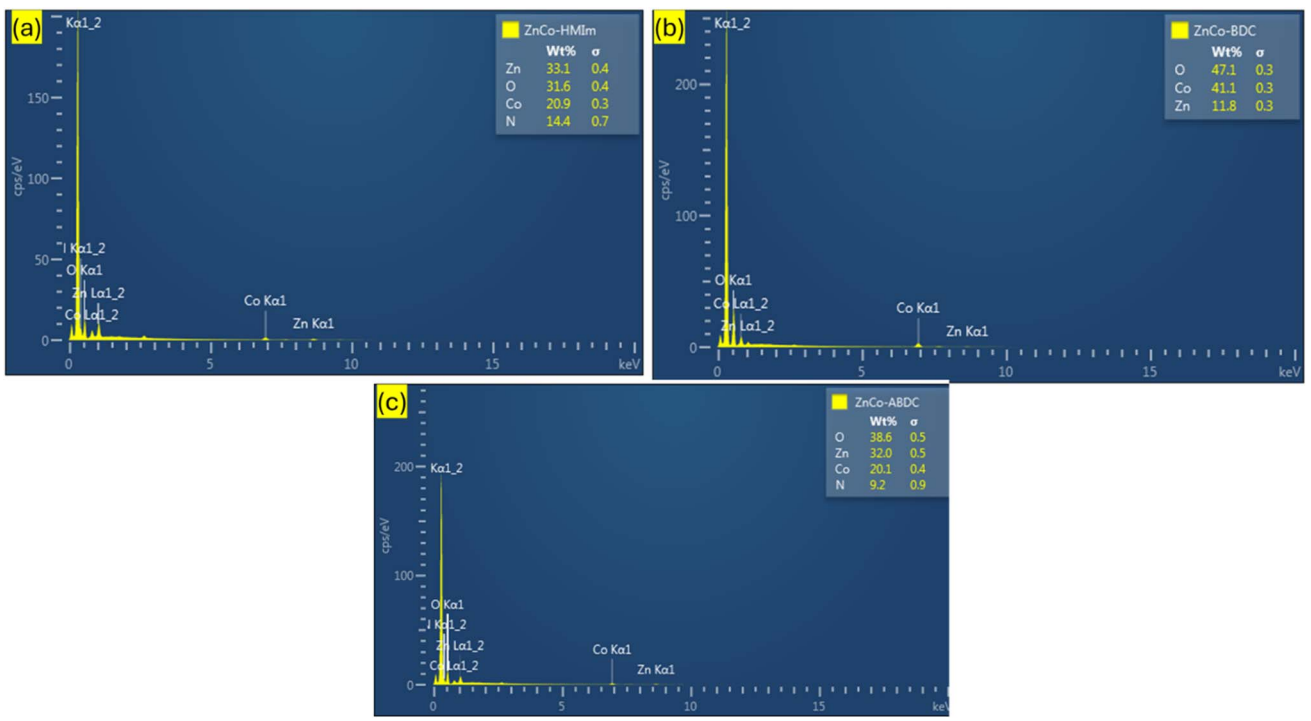

Fig. 4 EDS spectra of the ZnCo-MOFs involving the three ligands (a) HMIM, (b) BDC and (c) ABDC.

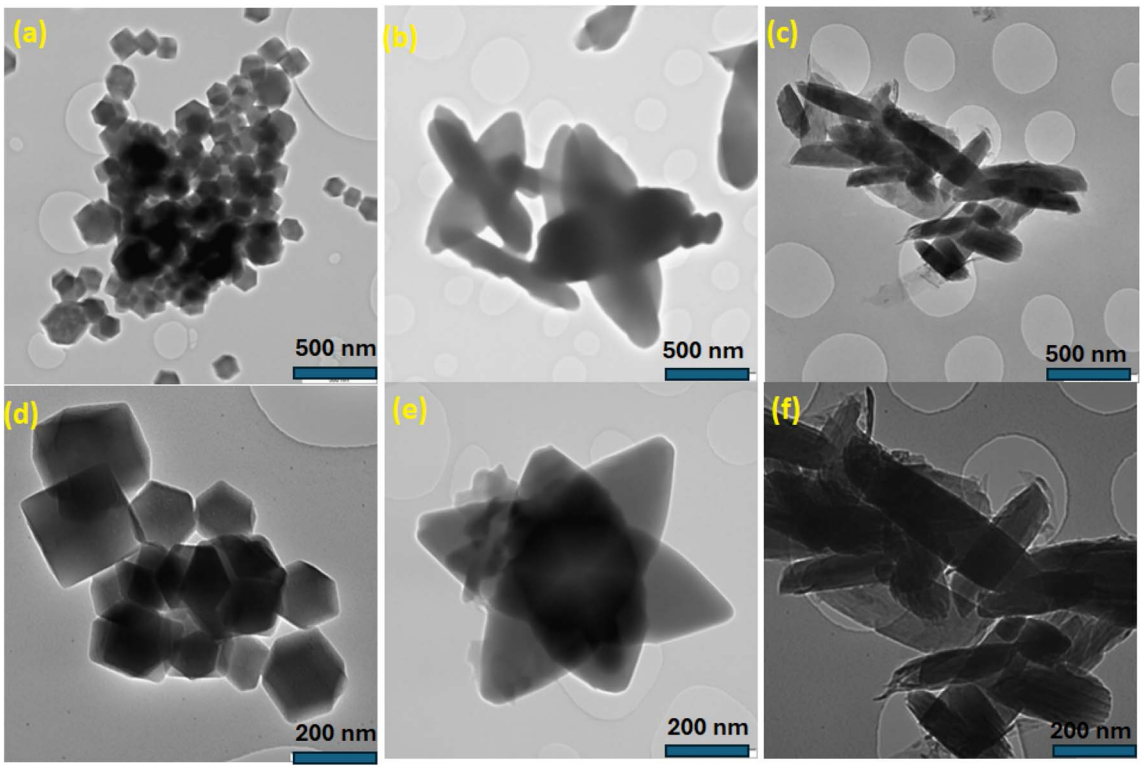

Fig. 5 (a–f) TEM micrographs of various magnifications of ligand mediated ZnCo-MOFs.

while ZnCo-MOF-ABDC rod-like shapes were shown in Fig. 5c, which are consistent with the SEM results. The results show that by varying the organic ligands in MOFs, it is possible to control the morphologies of the bimetallic ZnCo-MOFs. The various interactions between the metal ions and the corresponding linkers during synthesis are primarily responsible for the various morphological MOFs.

Based on the above results and discussion, the possible formation mechanism of ZnCo-MOFs can be explained as follows: due to the deprotonation and nucleation rates of 2-methylimidazole in a mixture of DMF and ethanol, the HMIM

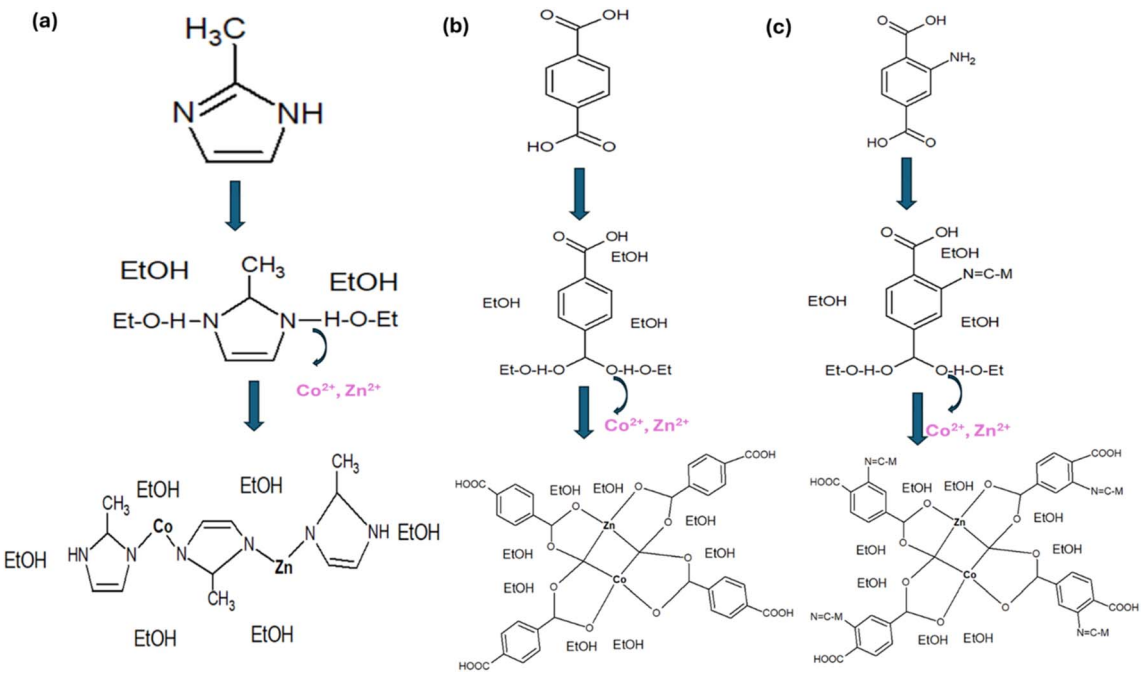

Fig. 6 Scheme showing the formation mechanisms of ZnCo-MOFs with (a) HMIM (b) BDC and (c) ABDC ligands.

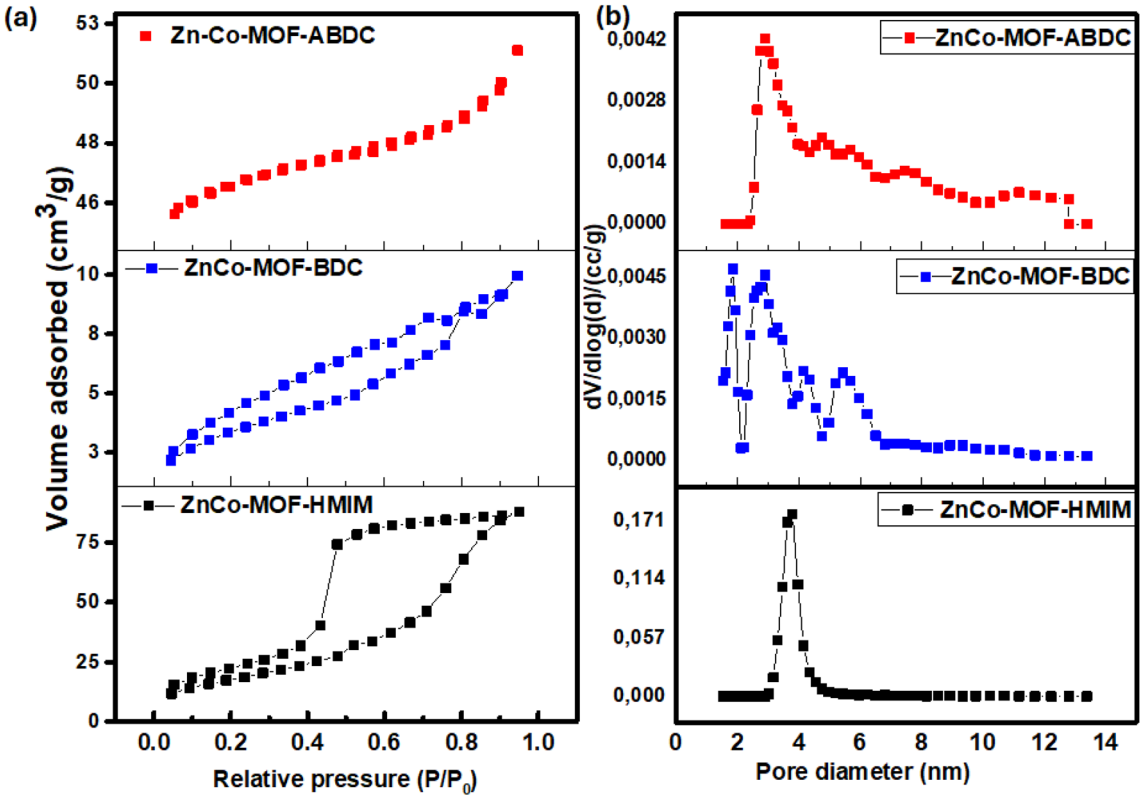

Fig. 7 (a) BET isotherms and (b) pore size distribution of ZnCo-MOFs prepared with different ligands.

ligand coordinates with appropriate metal ions (Co^{2+} or Zn^{2+}) to generate dodecahedron ZnCo-MOF–M═HMIM (Fig. 6a). The C–O bond of NH_2–H_2BDC combines with its NH_2 to generate a C–N bond when it is dissolved in a mixture of DMF and ethanol. The resultant ligands subsequently coordinate with the metal ions to form NiCo-MOFs. The C–N bond facilitates the development of a rod-like structure in this mechanism (Fig. 6c). By contrast, only elliptical cross-like structures are produced when 1,4-terephthalic acid (H_2BDC) is substituted for NH_2–H_2BDC during the synthesis process of NiCo-MOF-BDC (Fig. 6b).

To obtain additional understanding of the pore structure and surface area of ZnCo-MOFs, Brunauer–Emmett–Teller (BET) measurements were conducted. Fig. 7a and b, respectively, display the isotherms and pore size distribution of ZnCo-MOF-HMIM, ZnCo-MOF-BDC, and ZnCo-MOF-ABDC. The surface area of the porous ZnCo-MOF-HMIM is 66.7 $m^2\ g^{-1}$, which is 5 and 4 times higher than those of ZnCo-MOF-BDC (12.9 $m^2\ g^{-1}$), and ZnCo-MOF-ABDC (15.1 $m^2\ g^{-1}$). A high surface area is very helpful in improving the electrolyte/electrode area, which creates more redox active sites for enhanced charge storage performance. The BJH total pore volumes (as shown in Table 1) for ZnCo-MOF-HMIM, ZnCo-MOF-BDC, and ZnCo-MOF-ABDC are 0.13, 0.01, and 0.08 $cm^3\ g^{-1}$, respectively. Additionally, ZnCo-MOF-HMIM displayed a typical type-IV isotherm indicating the presence of mesopores with a homogeneous pore-size distribution,[34] as illustrated in Fig. 7b. These mesopores provide good electrolyte access in addition to a suitable electrochemical activity center for outstanding supercapacitor performance.

X-ray photoelectron spectroscopy (XPS) technique was used to obtain the elemental composition and chemical states on the ZnCo-MOF-HMIM. The components of the ZnCo-MOF-HMIM are consistent with the survey spectra, which indicate the presence of Zn, Co, O, N and C elements as depicted in Fig. 8a. The successful coordination of Zn^{2+} and Co^{2+} with the HMIM ligand was further evidenced by the emergence of Zn 2p peak and Co 2p peak in the survey spectrum of ZnCo-MOF-HMIM. The presence of Zn^{2+} in ZnCo-MOF-HMIM is implied by the XPS spectrum of Zn 2p (Fig. 8b), where the primary peak at 1021.1 eV is attributed to the binding energy of Zn $2p_{3/2}$ and the peak at 1043.9 eV is assigned to Zn $2p_{1/2}$. The peaks at 780.4 eV and 795.9 eV in the high resolution XPS spectra of the Co 2p in ZnCo-MOF-HMIM (Fig. 8c) were identified as Co $2p_{3/2}$ and Co $2p_{1/2}$ of Co^{2+} in ZnCo-MOF-HMIM, respectively, while the binding energies at 801.98 and 786.12 eV are the satellite peaks corresponding to the Co^{2+} oxidation state. The binding energies of C 1s (Fig. 8d) were deconvoluted into three peaks, corresponding to C═C C–N and C═O, at 284.1, 285.5 and 290.8 eV, respectively. The O 1s spectra (Fig. 8e) showed that the majority of the O in the sample was present as H_2O, with the binding energies of H–O–H and –OH located at 533.2 eV and 531.6 eV, respectively. Furthermore, it was determined that the Co–N and Zn–N, which came from the imidazolate structure, were responsible for the peaks in Fig. 8e at 398.3 and 397.6 eV, respectively. The N 1s spectra identified NO_3^-, which could be

Table 1 Performance comparison of bimetallic Co-based MOFs in half-cell with the present study

Electrode	Parent MOF	Electrolyte	Specific current ($A\ g^{-1}$)	Specific capacity ($m\ h\ A\ g^{-1}$)	Capacity retention (%)/cycle number	Ref.
Co-MOF/PANI	Co-MOF	1 M KOH	0.4	45	146/3000	44
Ni/Co-MOF	Co-MOF	2 M KOH	1.0	94.2	70/2000	45
ZIF-67@300	Co-MOF	6 M KOH	1.0	94.1	64/5000	46
NiCo-MOF	Co-MOF	2 M KOH	1.0	157.8	75/3000	17
NiCo-S-0.5/NC	Co-MOF	3 M KOH	1.0	151.1	80/3000	47
ZnCo-MOF/GS	Co-MOF	3 M KOH	1.0	115.8	80/7500	48
Ni,Co-MOF	Co-MOF	3 M KOH	1.0	81.1	89/3000	49
Co-MOF/PANI	Co-MOF	1 M KOH	1.0	70.2	90/5000	50
Zn-MOF/rGO	Zn-MOF	1 M H_2SO_4	0.1	51.6	77/5000	51
ZnCo-MOF-HMIM	Co-MOF	6 M KOH	1.0	176.8	88/5000	This work
ZnCo-MOF-BDC	Co-MOF	6 M KOH	1.0	66.7	71/5000	This work
ZnCo-MOF-ABDC	Co-MOF	6 M KOH	1.0	102.6	78/5000	This work

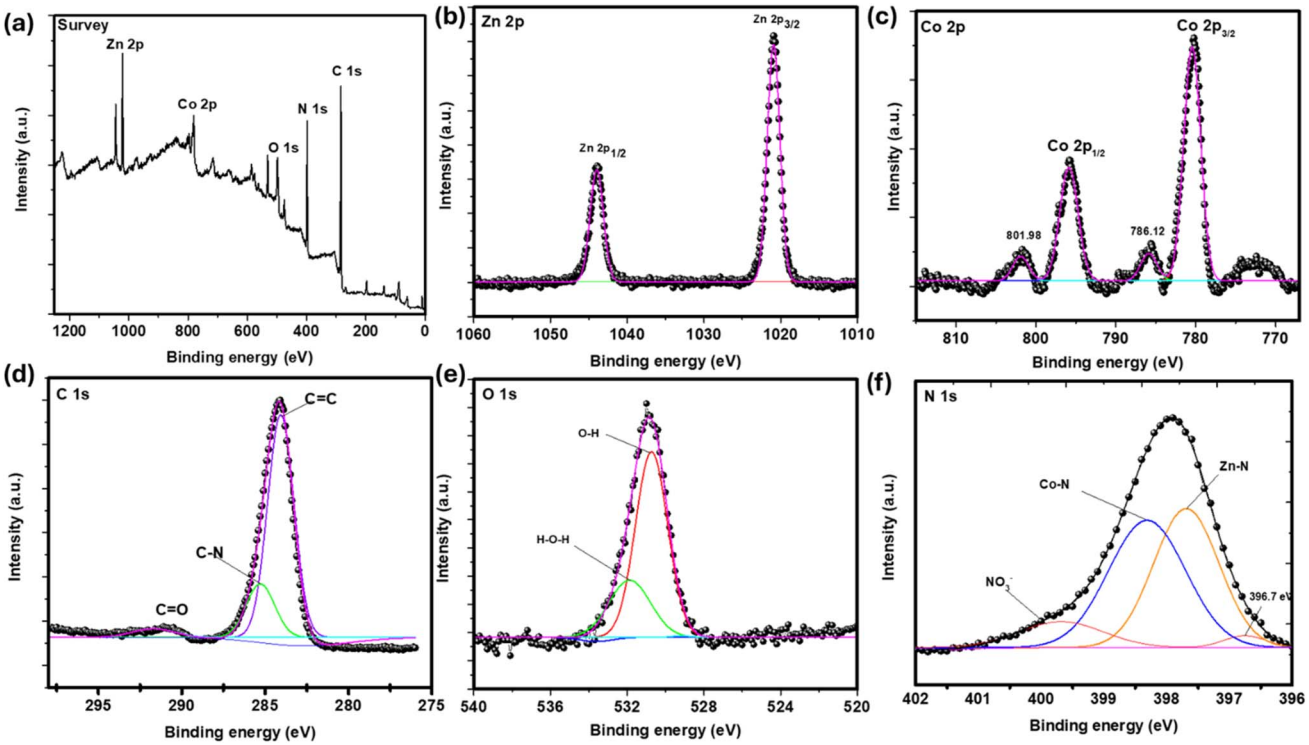

Fig. 8 (a) XPS survey spectrum of ZnCo-MOF-HMIM, and high-resolution XPS spectra of (b) Zn 2p (c) Co 2p (d) C 1s (e) O 1s and (f) N 1s.

from cobalt nitrate hexahydrate, as the weak and broad peak at about 400.0 eV which is consistent with the work of Hu *et al.*[35]

Ultraviolet-visible spectroscopy explains the band gap (E_g) of the ZnCo-MOFs modified by different ligands.[36] The UV-vis spectra shows that the bimetallic MOF samples exclusively exhibit two prominent bands at different wavelengths (Fig. 9). These are attributed to the n–π^* transition, which involves the single electron pair from the ligand, and the overlap of the linker's π–π^* transitions with the M–O or M–N (M = Zn and Co) cluster absorption bands, respectively (Fig. 9). The π–π^* transition in the HMIM ligand could be connected to the significant absorption peaks in the UV region 306 nm which is more intense than BDC (229 nm) and ABDC (246 nm). The observed difference might be brought on by the different metal to linker (M–L) interactions. The interactions between bimetallic metal ions and N and O atoms (from the linkers) were confirmed to be the source of the valence band (VB) or conduction band (CB) nature in the three bimetallic MOFs modified by ligand effect.[37] This gives rise to VB, which is largely consist of oxygen or nitrogen 2p orbitals, and CB, which is primarily composed of Zn and Co 3d orbitals. The semiconductor characteristics of ZnCo-MOFs are determined by the energy gap between these bands.[56,57] Since Zn and Co have been coordinated to the linkers in a different manner due to the difference in their electronic structures, different band gaps were obtained ZnCo-MOF-HMIM, ZnCo-MOF-BDC, and ZnCo-MOF-ABDC. Tauc's equation eqn (4) was used to evaluate the E_g of the samples:[38]

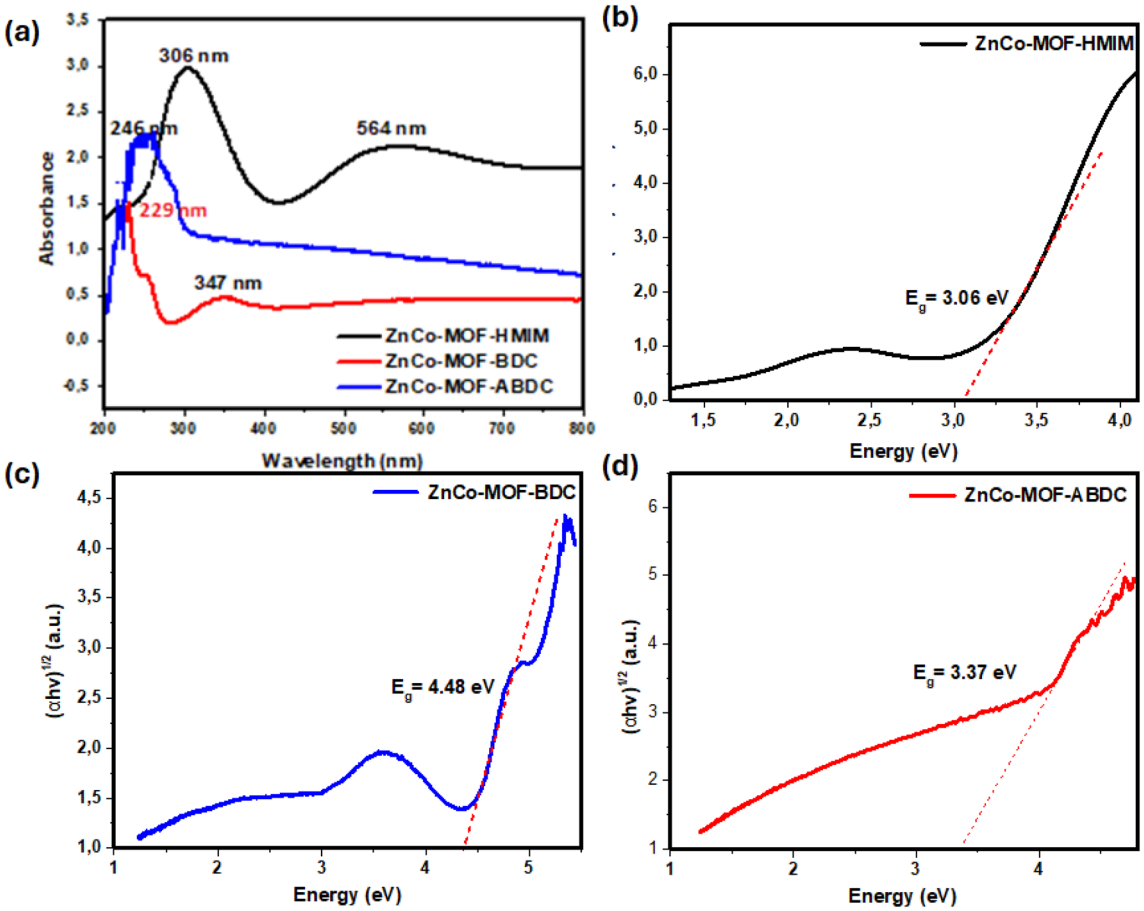

Fig. 9 (a) UV-visible spectra and (b–d) band gap plots of ligand-modified Zn Co MOFs.

$$\alpha h\nu = A\left(h\nu - E_g\right)^{\frac{n}{2}} \quad (4)$$

where, in that order, h, α, ν, A, and E_g stand for the optical band gap, Planck's constant, constant of proportionality, incident light frequency, and absorption coefficient respectively. The value "n" also represents the several kinds of attenuated electronic transitions that can occur; $n = 1$, 3, 4, & 6 are permissible direct transitions, banned direct transitions, allowed indirect transitions, and forbidden indirect transitions, respectively. The ligand-modified bimetallic ZnCo-MOF showed permitted indirect transition ($n = 2$) in the present circumstance. Accordingly, the E_g values in the bimetallic ZnCo-MOF-HMIM, ZnCo-MOF-BDC, and ZnCo-MOF-ABDC were found to be 3.06, 4.48, and 3.37 eV respectively (Fig. 9b–d). The N donor in the imidazole ring of HMIM contributed to the electronic organization of ZnCo-MOF-HMIM and enhanced its E_g value. The structural architecture, electronegativity of the heteroatoms from the linkers, and the extent of valence electron delocalization were identified as the causes of the variances in E_g values.

Given the above characterization results, it can be deduced that coordination bonds are the main mechanism by which metal ions/nodes and ligands interact in MOFs. The structural integrity of MOFs under a variety of circumstances is determined by its coordination ability. Thus, it is essential to select ligands with appropriate functional groups and structural features that give high framework stability.

3.1 Electrochemical performance of ligand-mediated ZnCo-MOFs

3.1.1 Three-electrode evaluation. A standard three-electrode cell configuration in a 6 M KOH electrolyte was deployed to evaluate the performance of the ZnCo-MOF electrode materials in supercapacitors. The CV curves of the synthesized materials were compared at 10 mV s^{-1} as shown in Fig. 10a. All the CV curves show symmetric oxidation-reduction peaks, demonstrating reversible redox activity. The peaks arise from the reaction between metal nodes and the electrolyte OH^- ions during the redox process. Due to the various contact areas and active metal sites, the redox-mediated reaction accounts for most of the performance.[39] Additionally, because of the quick surface redox reaction, the ligands in the MOF matrix participate in the chemical reaction to some extent and contribute some pseudocapacitance. The ligands (HMIM, BDC and ABDC) contain –NH–COOH and $–NH_2$ groups, which are responsible for this contribution. Stemmler *et al.* reported the OH^- radical facilitated oxidation of organic compounds in an aqueous solution and suggested possible reaction mechanism. Accordingly, the following list of potential reactions is provided, where

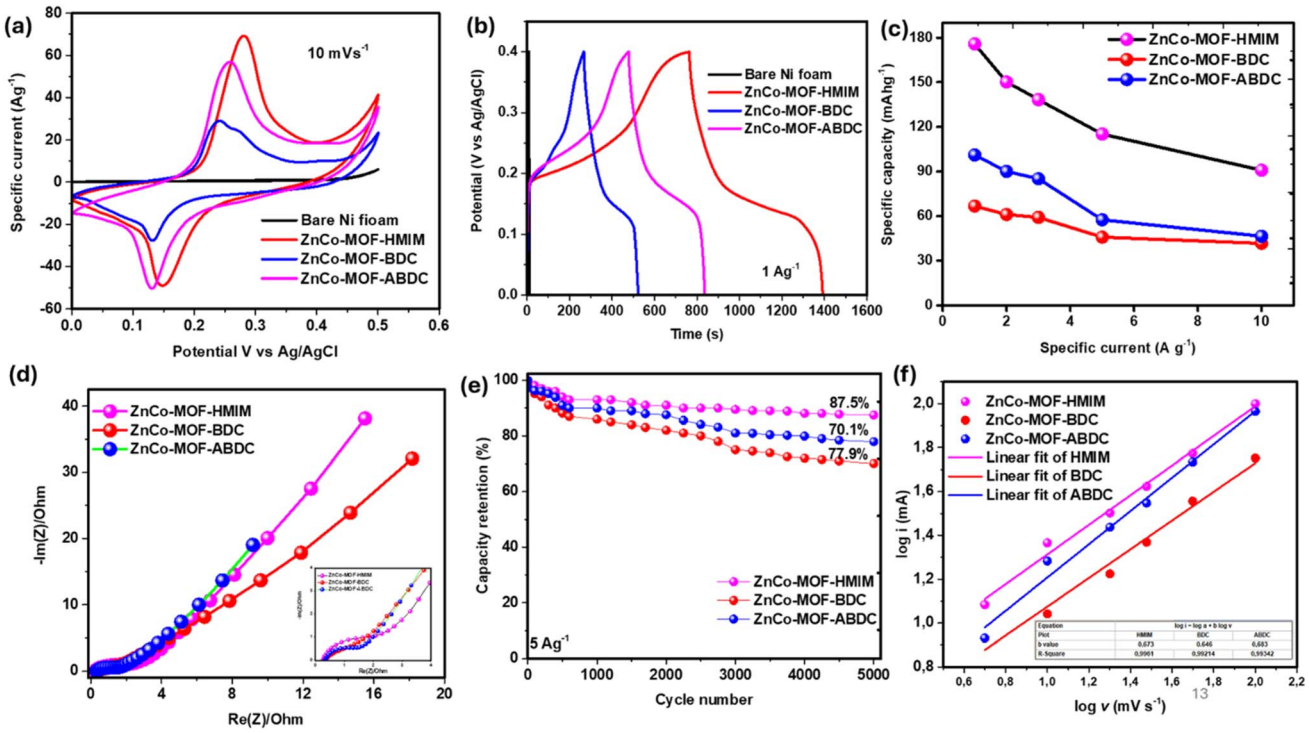

Fig. 10 (a) CV curves of ZnCo-MOFs at 10 mV s^{-1}, (b) GCD curves of ZnCo-MOFs at 1 A g^{-1}, (c) the specific capacity at various specific currents, (d) Nyquist plots and (e) cycling stability at 5000 cycles of ZnCo-MOFs at 10 A g^{-1} (f) plot of log of the current *vs.* scan rate.

R stands for the hydrogen and carbon radical groups found in the ligand metallic framework.

$$R\text{–}NH + OH^- \rightleftharpoons \text{–}R\text{–}N + H_2O + e^-$$

$$R\text{–}COOH + OH^- \rightleftharpoons \text{–}R\text{–}COO + H_2O + e^-$$

$$R\text{–}NH_2 + OH^- \rightleftharpoons \text{–}R\text{–}NH + H_2O + e^-$$

When compared to the other electrodes, ZnCo-MOF-HMIM exhibits the biggest CV curve area, indicating higher charge storage performance than the other ZnCo-MOFs. The Zn^{2+} and Co^{2+} ions penetrate the MOF to synergize the bimetallic active sites through the unique coordination capabilities of the Zn and Co ions, and N donor atoms from the imidazole ligand. Which combines high hydrophobicity, large specific surface area, as well as large and uniform pore size. The high performance of ZnCo-MOF-HIM is consistent with the unique chemistry of its ligand, surface and structural morphology and high specific surface area which speeds up charge transfer and increases the active surface area. The introduction of cobalt ions in ZnCo-MOF enhances the pseudocapacitive mechanism and improves electrochemical performance. This was confirmed through a GCD test on electrode materials carried out in the potential voltage range of 0.0–0.4 V. Notably, the ZnCo-MOF-HMIM sample has the longest charge–discharge time, resulting in the highest specific capacity of 176.8 mA h g^{-1} at 1 A g^{-1}, compared to ZnCo MOF-BDC (66.7 mA h g^{-1}) and ZnCo MOF-ABDC (102.6 mA h g^{-1}) at the same specific current (Fig. 10b). Fig. 10c is a plot of the specific capacity as a function of the specific current. The corresponding Nyquist plots from the EIS are displayed in Fig. 10d. These Nyquist plots were primarily made up of a straight line in the low frequency zone and a semicircle at the high frequency region and offers valuable information regarding charge dynamics and electrical conductivity and interfacial properties of the ZnCo-MOFs.[40] The inset displays the ESR values that correlate to the high frequency real impedance intercept at 0.26, 0.37, and 0.32 Ω for HMIM, BDC and ABDC-based MOFs, respectively. Given the ZnCo-MOF-HMIM's high number of electrochemical active sites, the decline in ESR is attributed to an expansion in the interactions of the chemical species involved. The transfer at the at the interface of electrode and electrolyte is further confirmed by the finding that ZnCo-MOF-HMIM has a R_{ct} of 1.48 Ω, which is smaller than that of the other ZnCo MOF-BDC (1.51 Ω) and ZnCo MOF-ABDC (1.67 Ω). Furthermore, the corresponding capacity retention values calculated after 5000 cycle number at 10 A g^{-1} using eqn (2) are found to be 87.5, 70.1, and 77.9% respectively for the HMIM, BDC and ABDC-based MOFs, respectively (Fig. 10e). Fig. S2† shows the GCD and EIS after 5000 cycles for the ZnCo-MOF-HMIM. Ligands that are resistant to decomposition or chemical degradation are more likely to contribute to the stability of the MOF.[41] The synergistic effect of the metal ions and framework stability gives the composite a much-improved capacity retention, while the bond strength formed by the imidazole –NH with the Zn and Co ions is responsible for the high-capacity retention value of ZnCo-MOF-HMIM compared to other ZnCo-MOFs. Owing to its exceptional electrochemical properties, ZnCo-MOF-HMIM was chosen for integration into hybrid device.

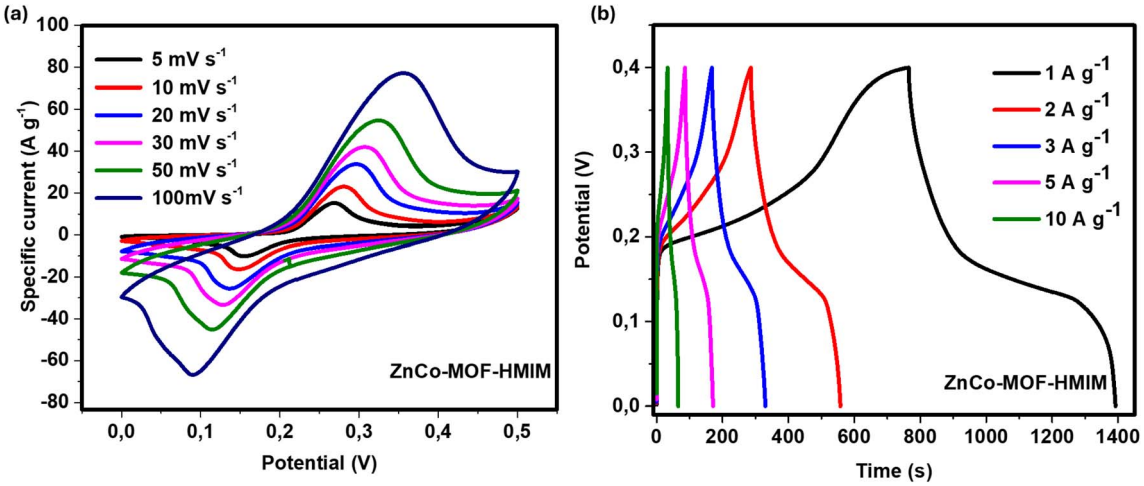

Fig. 11 (a) CV curve of ZnCo-MOF-HMIM at different scan rates and (b) GCD curve of ZnCo-MOF-HMIM at different specific currents.

Detailed electrochemical characterization was carried out on ZnCo-MOF-HMIM owing to its superior performance. In Fig. 11a, the electrode was subjected to CV at various scan rates up to 100 mV s^{-1}. The linear enhancement in the CV profile area with scan rate is an indication of good rate capability of the HMIM-based MOF. Moreover, the peaks for Zn and Co are the same since they oxidize at the same potential. The following reversible reactions are responsible for the redox reaction:

$$Zn(II) + OH^- \rightleftharpoons Zn(II)(OH) + e^-$$

$$Co(II) + OH^- \rightleftharpoons Co(II)(OH) + e^-$$

Interestingly, the ZnCo-MOF-HMIM maintained its shapes at different tested scan rates, showing good stability, with anodic and cathodic peaks resembling a faradaic behavior. The increased transport impedance linked to electrolyte ions causes the reduction and oxidation peaks to move to greater and less significant potentials at high scan speeds. Less oxidation peak area was caused by internal active sites, which led to fewer redox reactions at higher scan speeds. In the same vein, a GCD test was conducted to analyze the behavior of ZnCo-MOF-HMIM at different specific currents (1.0–10.0 A g^{-1}) as shown in Fig. 11b. The potential fluctuated nonlinearly over time, displaying platforms for charging and discharging similar to standard battery electrodes. The decrease in the discharge time with specific current can be attributed to quick current reactions to possible reversals and fast ion diffusion.

To get additional insight into the mechanism by which the charges are stored, the kinetics of the ZnCo-MOF electrodes was investigated. First, eqn (5) was adopted to evaluate the materials for their surface and diffusion contributions.[42]

$$i(V) = av^b \quad (5)$$

Eqn (5) can be linearized to give eqn (6):

$$\log i = \log a + b \log v \quad (6)$$

where a, b are arbitrary constants, v is the scan rate, and $i(V)$ is the peak current at a fixed potential. The b-values computed at peak potentials from the plot of log i against log v of ZnCo-MOFs from HMIM, BDC and ABDC are respectively 0.67, 0.64 and 0.68 respectively as shown in Fig. 11f. The b values which is far less than 1 implies that both the capacitive and diffusion mechanisms cooperate during storage and that diffusion mechanism predominates in all the three ligand-modified ZnCo-MOFs. Furthermore, eqn (7) provided by Dunn method were applied to fine tune the actual contributions of each process of the best performing electrode (ZnCo-MOF-HMIM):[43]

$$i(V) = k_1 v + k_2 v^{1/2} \quad (7)$$

where k_1 and k_2 are arbitrary constants, i is the current, and the terms $k_1 v$ and $k_2 v^{1/2}$ represent surface and diffusion processes, respectively. The values of k_1 and k_2 can be gotten from the gradient and the y-intercept, respectively, of the plot of $\frac{i(V)}{v^{\frac{1}{2}}}$ against $v^{1/2}$.

The charge contributions of the ZnCo-MOF-HMIM at various scan rates are displayed in Fig. 12a. According to the data, both surface and diffusion are involved in the charge storage mechanism. The diffusion and surface contributions are 81% and 19%, respectively, at 5 mV s^{-1} and 48% and 42% at 50 mV s^{-1} and 49% and 51%, respectively, at maximum scan rate of 100 mV s^{-1}, as further illustrated in Fig. 12b–d. This confirms that the ZnCo-MOF-HMIM electrode in the basic electrolyte is a supercapacitor of the battery type.

The performance of electrodes based on bimetallic MOFs composites that have been published in the literature are contrasted in Table 1. In this study, ZnCo-MOF-HMIM produced the maximum specific capacity of 176.8 mA h g^{-1} at 1 A g^{-1} with stability of 87.5% after 5000 charge–discharge cycles. The remarkable performance of this material can be linked to the ample space within its crystal structure, which facilitates both the quick movement of ions and the diffusion and storage of the electrolyte ion. As a result, these structures possess exceptional

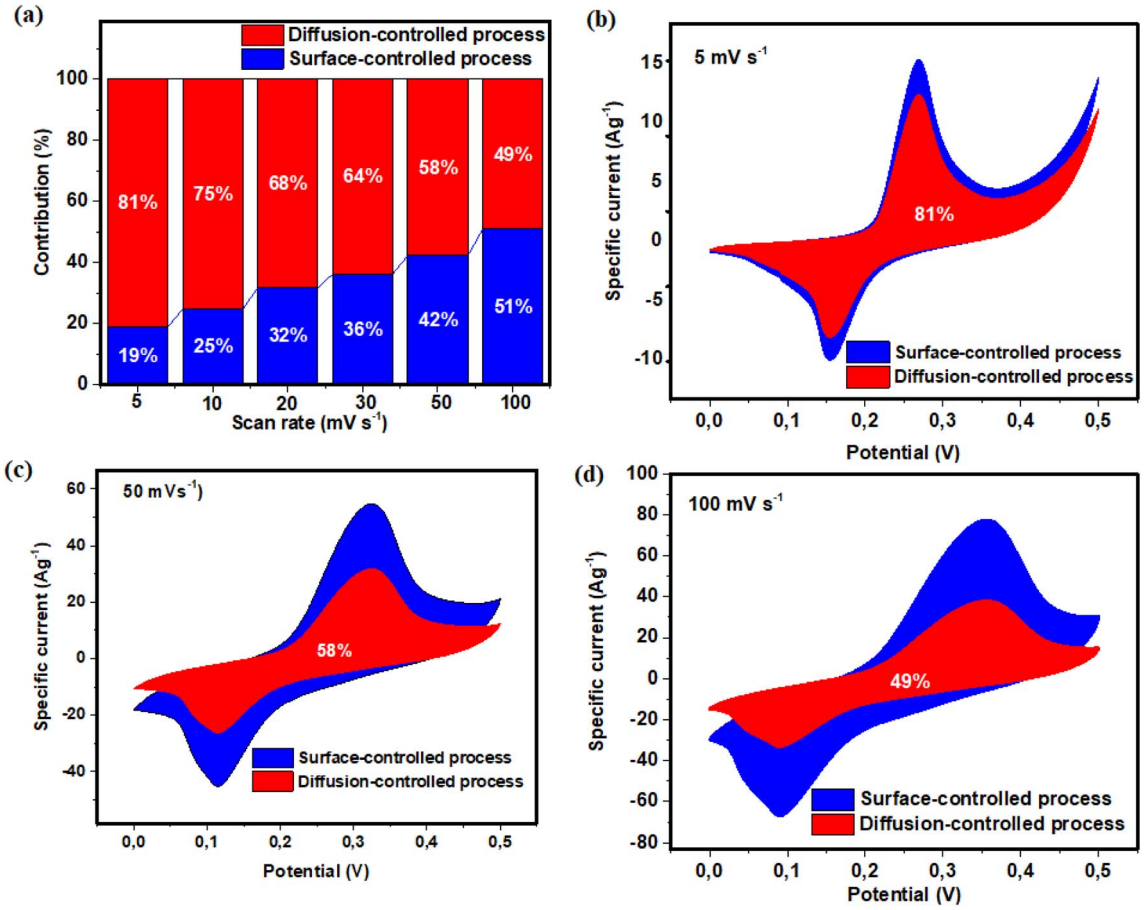

Fig. 12 (a) Contributions of charge storage mechanisms against scan rate, CV curves with displaying contributions of each process at (b) 5 mV s^{-1}, (c) 50 mV s^{-1} and (d) 100 mV s^{-1} of ZnCo-MOF-HMIM.

electrochemical properties as a supercapacitor material. It was observed that the capacity retention value obtained for the ZnCo-MOF-HMIM is comparable to those obtained from other bimetallic MOFs owing to the high stability of the imidazole ligand when coordinated with the bimetallic Zn and Co ions.

3.1.2 Two-electrode measurement. For practical applicability, the ZnCo-MOF-HMIM was tested in an asymmetric supercapacitor device containing 6 M KOH electrolyte where activated carbon (PAC) obtained from peanut shell serves and ZnCo-MOF-HMIM serve as positive and negative electrodes respectively. The charge in each electrode was balanced to avoid a situation in which one electrode would eventually charge the other. To accomplish this, the ratio of the electrodes based on their masses was calculated using the mass balance using eqn (8).

$$\frac{m_+}{m_-} = \frac{C_{S-} \times V_{S-}}{3.6 Q_{S+}} \quad (8)$$

The masses of the negative and positive electrodes (mg) are represented as m_- and m_+ correspondingly. The negative electrode's specific capacitance (F g^{-1}) is given as C_{S-}, whereas the positive electrode's specific capacity (mA h g^{-1}) is Q_{S+}. V_{S-} is the potential of the negative electrode (V). The coated masses were 3.2 mg cm^{-2} and 0.8 mg cm^{-2} for the negative and positive electrodes, respectively. This corresponds to a 4 : 1 mass ratio of m_-/m_+. As a result, it was estimated that the device's electrode mass was 4.0 mg cm^{-2}.

The CV curve of the hybrid device at different scan rates (up to 100 mV s^{-1}) is displayed in Fig. 13a. The EDLC characteristics are seen in a cell potential range of roughly 0–0.8 V. The potential range of 0.8 to 1.6 V is where the faradaic behavior is most noticeable. This demonstrates that the device benefits from the positive and negative electrodes at lower and higher cell potentials, respectively. On the other hand, the redox peaks vanish as the scan rate rises, confirming the composite material's shift from faradaic to pseudocapacitive nature. The device's integration of the EDLC material is responsible for this. In Fig. 13b, the GCD is displayed at a particular current between 1 and 10 A g^{-1}. The symmetry of the curves illustrates the reversibility of the redox reactions. Since the GCD curves lack distinct horizontal plateaux, the charge storage mechanism is pseudocapacitive rather than EDLC or fully faradaic. Fig. 13c illustrates the change in specific capacity with specific current from 1 to 10 A g^{-1}. The maximum specific capacity at 1 A g^{-1} is 27.4 mA h g^{-1}, while the equivalent rate capability at 10 A g^{-1} is 49%. Using the equivalent circuit in the inset, Fig. 13d displays the experimental results of the device and the fitting line of the

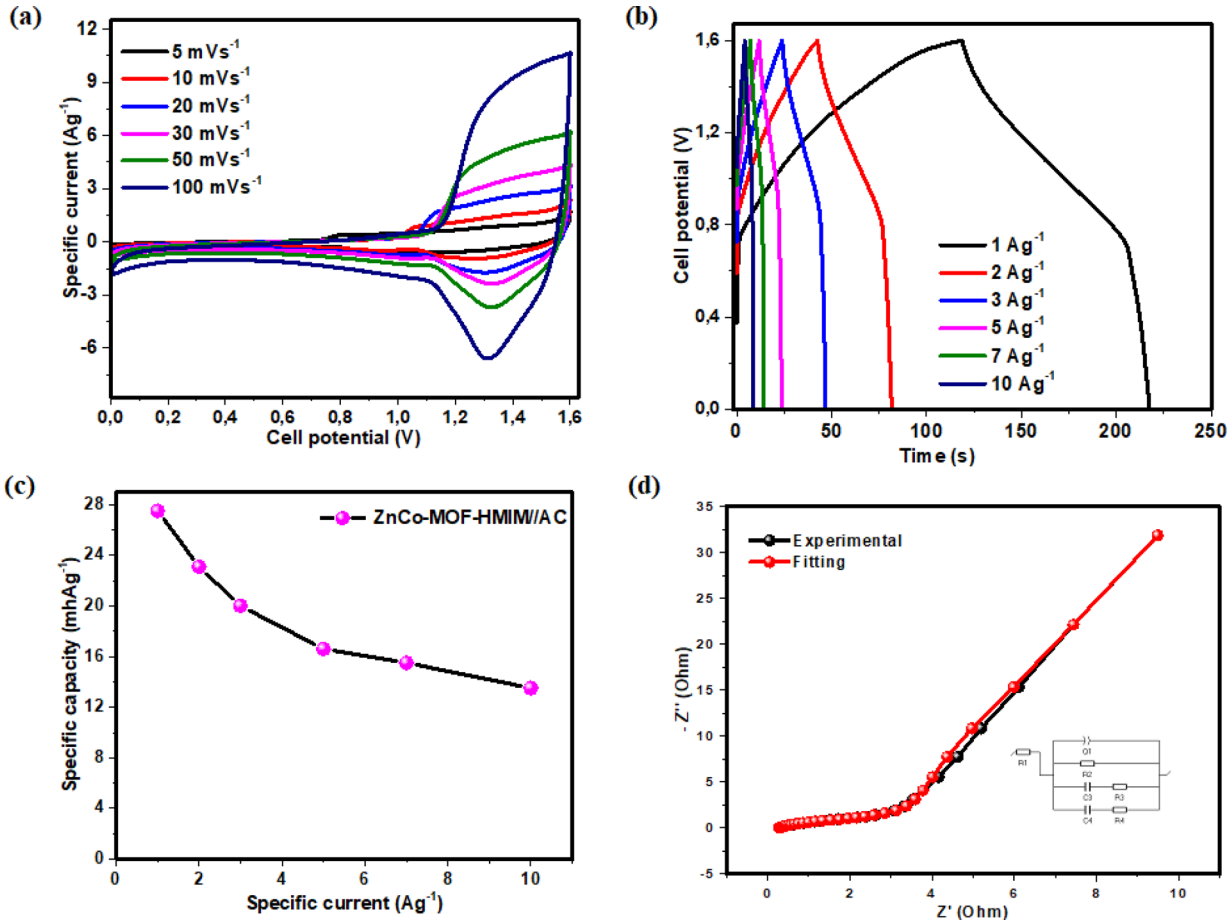

Fig. 13 (a) CV plots of the device at various scan rates, (b) GCD at different specific currents, (c) the specific capacity *vs.* specific current and (d) Nyquist plot of the experimental data with the fitting curve and the equivalent circuit in the inset.

Nyquist plot. The fitting curve's ESR value was 0.278 Ω, but the experimental curve's was 0.275 Ω. The device's Nyquist plot shows a very noticeable semicircle, which is caused by the charge transfer resistance (R_{ct}: 2.9 Ω) at the electrode and electrolyte interface in the high-frequency zone.

Fig. 14a displays the Ragone plot, which was calculated using eqn (2) and (3) to demonstrate the specific energy and specific power of the device incorporating ZnCo-MOF-HMIM. With a specific energy of 28.2 W h kg^{-1} at a specific power of 1025 W kg^{-1}, the dodecahedron-like ZnCo-MOF-HMIM//AC device has a higher specific energy than some published Zn-MOF and Co-MOF based materials, as indicated in Table 2. The device's stability at various charge–discharge cycles is shown in Fig. 14b. At 10 A g^{-1}, the device maintained a coulombic efficiency of 98.4% and a capacity retention of 80.0% after 10 000 GCD cycles. The coulombic efficiency (Fig. S3†) first rises then drops with an increase in the specific current, which can be linked to the inner active sites of the electrode material that cannot sustain the redox reaction at high specific currents. Kubra *et al.*[52] The stability is remarkable because of the imidazolate building block, the framework stability, and the synergistic effect of the constituting materials, which allowed for excellent electrochemical stability and good charge transport channels.[53]

The Nyquist plots before and after cycling are displayed in Fig. 14c. The two curves are nearly identical after 10 000 GCD cycles, suggesting that the imidazole ligand's conjugated structure remains intact under various charge–discharge cycles. However, a decrease in the rate of transport and transfer of electron and electrolyte ions through the bulk of the composites and at the interface between the electrode and electrolyte may be the cause of the slopes of the straight line and the increase in R_{ct} values in the low frequency region. The CV curve (Fig. 14d), which shows no discernible change in the CV curve area after 10 000 cycles, further supports the stability of the assembled device. Fig. 14e displays the phase angle as a function of frequency using the Bode plot. This indicates that the device possesses both faradaic and capacitive properties. The phase angle in the low frequency band is −73°, which is not very near to −90°. Fig. 14f displays the device plot of the real (C') and imaginary (C'') capacitances against the frequency. The relaxation time, or the amount of time needed to fully charge the supercapacitor, peaked at 0.07 Hz and was as low as 2.4 s. This demonstrates that the ZnCo-MOF-HMIM's improved ion diffusion leads to remarkable rate performance at high charge–discharge rates. Because of its distinct textural characteristics, which improve the ion transport capabilities, it achieves an

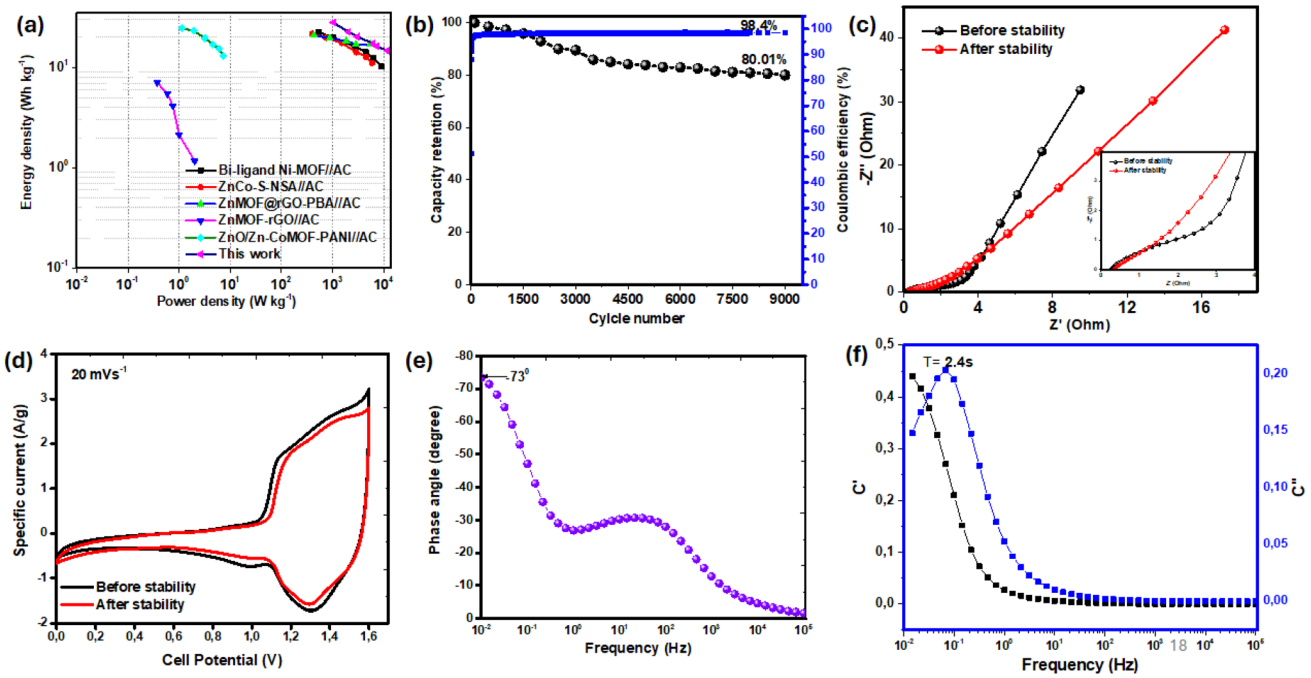

Fig. 14 (a) Ragone plot of the device, (b) cycling stability test after 10 000 cycles at 10 A g^{-1}, (c) Nyquist plot with an inset showing high frequency zone magnification before and after cycle stability, (d) CV plots before and after stability, (e) Bode plot and (f) imaginary and real capacitance *vs.* frequency of the hybrid device.

Table 2 Performance comparison of ZnCo-MOF//AC in two electrodes with relevant MOF composites in the literature

Electrode	Cell potential (V)	Electrolyte	Specific energy (W h kg^{-1})	Specific power (W kg^{-1})	Ref.
CoNi-MOF//AC	1.45	1 M KOH	26.8	1450	55
NiCo-MOF/MWCNT/MWCNT	1.0	2 M KOH	19.7	250	56
ZIF-8/melamine (ZM-C-800)//AC	1.0	6 M KOH	16.4	249.1	57
ZIF-8/PP-SiO_2//AC	1.6	1 M Na_2SO_4	13.3	—	58
ZnO–ZnCo/MOF PANI//AC	1.45	6 M KOH	26	725	59
Co–Ni–MOF//AC	1.6	6 M KOH	21.9	348.9	60
Co-MOF/PANI//AC	1.6	1 M KOH	23.2	1600	44
NiCo-MOF//AC	1.3	2 M KOH	12.8	372.5	45
ZnCo-MOF-HMIM//AC	1.6	6 M KOH	28.2	1025.4	This work

impressive conductivity at the electrode–electrolyte interface. The improved surface chemistry brought about by the ligand stability integrated into the MOF framework and the combined effects of the two metal ions in increasing the conductivity of the bimetallic MOF are directly responsible for this remarkable performance.[54]

4. Conclusions

In conclusion, a facile one-pot solvothermal synthesis approach was effectively used to probe the ligand effect on the physicochemical properties of bimetallic ZnCo-MOFs for supercapacitor applications. ZnCo-MOFs with different morphologies such as dodecahedron, cross elliptical sheets, and rod shapes are obtained by altering the ligands in the bimetallic MOFs. The interaction of Zn^{2+} and Co^{2+} metal ions with the linkers and solvent molecules leads to various structures of ZnCo-MOFs. Compared to other ZnCo-MOFs, the bimetallic ZnCo-MOF-HMIM had the largest specific capacity, measuring 176.8 mA h g^{-1} at 1 A g^{-1}. After 5000 cycles, 87.5% of the initial capacity was retained in a three-electrode cell configuration. The π–π interactions between imidazole rings in the organic ligands constituting ZnCo-MOF-HMIM provided an enhancing stability. These interactions strengthen the framework's resistance to structural modifications and contribute to its overall performance. Besides, at a specific power of 1025 W kg^{-1}, the fabricated ZnCo-MOF-HMIM//AC asymmetric device afforded a specific energy of 28.2 W h kg^{-1}. After 10 000 cycles, 80.0% of the capacity was still retained. This study not only reveals empirical evidence supporting the impacts of ligand composition on the formation of mechanisms of bimetallic ZnCo-MOFs for supercapacitor but also will create

opportunities for the design of bimetallic MOFs for enhanced electrochemical performance.

Data availability

All the data used for this work are within the article and supporting documents. Further inquiries can be directed to the corresponding author.

Author contributions

Kabir Otun and Ncholu Manyala conceived the idea. All authors contributed equally to this work. All authors have discussed the results, read the manuscript and agreed with its content. Ncholu Manyala, Oladepo Fasakin, Ndeye Fatou Diop, and Rashed Ali Mohamed Adam edited the manuscript. All authors examined the results, read the manuscript and unanimously agreed with its content.

Conflicts of interest

There are no conflicts to declare.

Acknowledgements

The authors are grateful for the support provided by the Sasol-NRF Innovation Fellowship Programme awarded through the University of Pretoria with grant number: SASPD22090956849.

References

1 J. Zhang, M. Gu and X. Chen, *Micro Nano Eng.*, 2023, **21**, 100229.
2 Y. Liu, Q. Wu, L. Liu, P. Manasa, L. Kang and F. Ran, *J. Mater. Chem. A*, 2020, **8**, 8218–8233.
3 M. Saleem, F. Ahmad, M. Fatima, A. Shahzad, M. S. Javed, S. Atiq, M. A. Khan, M. Danish, O. Munir, S. M. Bin Arif, U. Faryad, M. J. Shabbir and D. Khan, *J. Energy Storage*, 2024, **76**, 109822.
4 F. Cheng, X. Yang, S. Zhang and W. Lu, *J. Power Sources*, 2020, **450**, 227678.
5 X. L. Su, S. Jiang, G. P. Zheng, X. C. Zheng, J. H. Yang and Z. Y. Liu, *J. Mater. Sci.*, 2018, **53**, 9191–9205.
6 S. Lv, L. Ma, X. Shen and H. Tong, *J. Electroanal. Chem.*, 2022, **907**, 116060.
7 P. Bhojane, *J. Energy Storage*, 2022, **45**, 103654.
8 C. Yuan, H. Xu, S. A. El-khodary, G. Ni, S. Esakkimuthu, S. Zhong and S. Wang, *Fuel*, 2024, **362**, 130795.
9 M. Xie, H. Lin, G. Liu, H. Yang, H. Hu, H. Dong, Y. Liu, X. Liu and Y. Xiao, *J. Energy Storage*, 2024, **96**, 112670.
10 K. O. Oyedotun and N. Manyala, *Curr. Opin. Electrochem.*, 2020, **21**, 125–131.
11 K. Yang, Q. Fan, C. Song, Y. Zhang, Y. Sun, W. Jiang and P. Fu, *GER*, 2023, **1**, 100030.
12 I. Pathak, D. Acharya, K. Chhetri, P. Chandra Lohani, T. Hoon Ko, A. Muthurasu, S. Subedi, T. Kim, S. Saidin, B. Dahal and H. Yong Kim, *Chem. Eng. J.*, 2023, **469**, 143388.
13 K. B. Wang, Q. Xun and Q. Zhang, *EnergyChem*, 2020, **2**, 100025.
14 K. O. Otun, M. S. Xaba, S. Zong, X. Liu, D. Hildebrandt, S. M. El-Bahy and Z. M. El-Bahy, *Colloids Surf., A*, 2022, **634**, 128019.
15 X. Chu, F. Meng, T. Deng, Y. Lu, O. Bondarchuk, M. Sui, M. Feng, H. Li and W. Zhang, *Nanoscale*, 2020, **12**, 5669–5677.
16 D. Tian, N. Song, M. Zhong, X. Lu and C. Wang, *ACS Appl. Mater. Interfaces*, 2020, **12**, 1280–1291.
17 X. Zhang, J. Wang, X. Ji, Y. Sui, F. Wei, J. Qi, Q. Meng, Y. Ren and Y. He, *J. Alloys Compd.*, 2020, **825**, 154069.
18 H. Yu, H. Xia, J. Zhang, J. He, S. Guo and Q. Xu, *Chin. Chem. Lett.*, 2018, **29**, 834–836.
19 D. You, H. Shi, L. Yang, P. Shao, K. Yin, H. Wang, S. Luo and X. Luo, *Chem. Eng. J.*, 2022, **435**, 134874.
20 Q. He, H. Zhao, Z. Teng, Y. Guo, X. Ji, W. Hu and M. Li, *J. Environ. Manage.*, 2024, **353**, 120149.
21 R. Murugan, V. Packirisamy and P. Pandurangan, *Mater. Sci. Semicond. Process.*, 2024, **179**, 108496.
22 M. Ćalasan, A. F. Zobaa, H. M. Hasanien, S. H. E. Abdel Aleem and Z. M. Ali, *J. Energy Storage*, 2021, **42**, 102998.
23 S. Zhang, N. Pan, S. Zhang and N. Pan, *Adv. Energy Mater.*, 2015, **5**, 1401401.
24 Y. Wang, H. Wang, J. Ye, L. Shi and X. Feng, *Chem. Eng. J.*, 2020, **383**, 123096.
25 X. Xu, K. Cao, Y. Wang and L. Jiao, *J. Mater. Chem. A*, 2016, **4**, 6042–6047.
26 S. Kaushik, P. Chand and S. Sharma, *J. Energy Storage*, 2024, **78**, 110033.
27 D. Aliyari, M. Mahdavian and B. Ramezanzadeh, *Mater. Today Chem.*, 2024, **38**, 102105.
28 V. Kumar, C. R. Mariappan, R. Azmi, D. Moock, S. Indris, M. Bruns, H. Ehrenberg and G. Vijaya Prakash, *ACS Omega*, 2017, **2**, 6003–6013.
29 W. Song, K. Ji, A. Aguadero, P. R. Shearing, D. J. L. Brett, F. Xie and D. J. Riley, *Energy Stor. Mater*, 2018, **14**, 324–334.
30 C. Healy, K. M. Patil, B. H. Wilson, L. Hermanspahn, N. C. Harvey-Reid, B. I. Howard, C. Kleinjan, J. Kolien, F. Payet, S. G. Telfer, P. E. Kruger and T. D. Bennett, *Coord. Chem. Rev.*, 2020, **419**, 213388.
31 H. Zhao, M. Li, J. Du, Y. Lei, A. Irfan, M. Imran, C. Wang, J. He, Z. Sun and P. K. Chu, *Electrochim. Acta*, 2023, **471**, 143366.
32 Y. si Hong, S. li Sun, Q. Sun, E. Q. Gao and M. Ye, *Mater. Chem. Phys.*, 2020, **243**, 122601.
33 M. H. Wang and S. P. Guo, *J. Alloys Compd.*, 2020, **832**, 154978.
34 L. Wang, B. Liu, S. Ran, H. Huang, X. Wang, B. Liang, D. Chen and G. Shen, *J. Mater. Chem.*, 2012, **22**, 23541–23546.
35 C. Hu, J. Xu, Z. Lu, C. Cao and Y. Wang, *Int. J. Hydrogen Energy*, 2021, **46**, 32149–32160.
36 W. Li, Y. Li, W. Zhang, D. Yin, Y. Cheng, W. Chu and M. Hu, *Chin. Chem. Lett.*, 2021, **32**, 1131–1134.
37 D. Wei, W. Tang, Y. Gan and X. Xu, *Catal. Sci. Technol.*, 2020, **10**, 5666–5676.

38 K. Baishya, J. S. Ray, P. Dutta, P. P. Das and S. K. Das, *Appl. Phys. A:Mater. Sci. Process.*, 2018, **124**, 1–6.
39 F. Zhang, M. Gao, S. Huang, H. Zhang, X. Wang, L. Liu, M. Han, Q. Wang, F. Zhang, M. Gao, S. Huang, H. Zhang, X. Wang, Q. Wang, L. Liu and M. Han, *Adv. Mater.*, 2022, **34**, 2104562.
40 S. D. Dhas, P. S. Maldar, M. D. Patil, K. M. Hubali, U. V. Shembade, S. B. Abitkar, M. R. Waikar, R. G. Sonkawade, G. L. Agawane and A. V. Moholkar, *J. Energy Storage*, 2021, **35**, 102277.
41 L. Feng, K. Y. Wang, G. S. Day, M. R. Ryder and H. C. Zhou, *Chem. Rev.*, 2020, **120**, 13087–13133.
42 T. Schoetz, L. W. Gordon, S. Ivanov, A. Bund, D. Mandler and R. J. Messinger, *Electrochim. Acta*, 2022, **412**, 140072.
43 R. Kumar and M. Bag, *J. Phys. Chem. C*, 2021, **125**, 16946–16954.
44 M. Z. Iqbal, M. M. Faisal, S. R. Ali, S. Farid and A. M. Afzal, *Electrochim. Acta*, 2020, **346**, 136039.
45 S. Sun, M. Huang, P. Wang and M. Lu, *J. Electrochem. Soc.*, 2019, **166**, A1799–A1805.
46 A. M. Kale, R. Manikandan, C. J. Raj, R. Velayutham, W. J. Cho and B. C. Kim, *Appl. Surf. Sci.*, 2021, **542**, 148716.
47 M. Yi, C. Zhang, C. Cao, C. Xu, B. Sa, D. Cai and H. Zhan, *Inorg. Chem.*, 2019, **58**, 3916–3924.
48 E. Erçarlkcl, K. Dağcl Klranşan and E. Topçu, *Energy Fuels*, 2022, **36**, 1735–1745.
49 Y. Jiao, J. Pei, D. Chen, C. Yan, Y. Hu, Q. Zhang and G. Chen, *J. Mater. Chem. A*, 2017, **5**, 1094–1102.
50 R. Srinivasan, E. Elaiyappillai, E. J. Nixon, I. Sharmila Lydia and P. M. Johnson, *Inorg. Chim. Acta*, 2020, **502**, 119393.
51 Q. B. Le, T. H. Nguyen, H. Fei, I. Sapurina, F. A. Ngwabebhoh, C. Bubulinca, L. Munster, E. D. Bergerová, A. Lengalova, H. Jiang, T. D. Tran, N. Bugarova, M. Omastova, N. E. Kazantseva and P. Saha, *Electrochim. Acta*, 2021, **367**, 137563.
52 K. T. Kubra, A. Javaid, R. Sharif, G. Ali, F. Iqbal, A. Salman, F. Shaheen, A. Butt and F. J. Iftikhar, *J. Mater. Sci.: Mater. Electron.*, 2020, **31**, 12455–12466.
53 Y. Cao, W. Yang, M. Wang, N. Wu, L. Zhang, Q. Guan and H. Guo, *Int. J. Hydrogen Energy*, 2021, **46**, 18179–18206.
54 N. Li, J. Xu, R. Feng, T. L. Hu and X. H. Bu, *Chem. Commun.*, 2016, **52**, 8501–8513.
55 X. Chu, F. Meng, T. Deng, Y. Lu, O. Bondarchuk, M. Sui, M. Feng, H. Li and W. Zhang, *Nanoscale*, 2020, **12**, 5669–5677.
56 X. Wang, N. Yang, Q. Li, F. He, Y. Yang, B. Wu, J. Chu, A. Zhou and S. Xiong, *J. Solid State Chem.*, 2019, **277**, 575–586.
57 C. Cai, Y. Zou, C. Xiang, H. Chu, S. Qiu, Q. Sui, F. Xu, L. Sun and A. Shah, *Appl. Surf. Sci.*, 2018, **440**, 47–54.
58 Z. Li, H. Mi, L. Liu, Z. Bai, J. Zhang, Q. Zhang and J. Qiu, *Carbon*, 2018, **136**, 176–186.
59 D. Qin, B. Zhou, Z. Li and C. Yang, *J. Mol. Struct.*, 2024, **1309**, 138140.
60 S. He, Z. Li, J. Wang, P. Wen, J. Gao, L. Ma, Z. Yang and S. Yang, *RSC Adv.*, 2016, **6**, 49478–49486.